Review of Scientific Instruments

A millikelvin scanning tunneling microscope in ultra-high vacuum with adiabatic demagnetization refrigeration

Cite as: Rev. Sci. Instrum. **92**, 063701 (2021); https://doi.org/10.1063/5.0050532
Submitted: 16 March 2021 • Accepted: 23 May 2021 • Published Online: 14 June 2021

Taner Esat, Peter Borgens, Xiaosheng Yang, et al.

Review of Scientific Instruments ARTICLE scitation.org/journal/rsi

A millikelvin scanning tunneling microscope in ultra-high vacuum with adiabatic demagnetization refrigeration

Cite as: Rev. Sci. Instrum. 92, 063701 (2021); doi: 10.1063/5.0050532
Submitted: 16 March 2021 • Accepted: 23 May 2021 •
Published Online: 14 June 2021

Taner Esat,[1,2] Peter Borgens,[1,3,a)] Xiaosheng Yang,[1,3] Peter Coenen,[1,4] Vasily Cherepanov,[1,4] Andrea Raccanelli,[5,a)] F. Stefan Tautz,[1,2,3] and Ruslan Temirov[1,6,b)]

AFFILIATIONS

[1] Peter Grünberg Institute (PGI-3), Forschungszentrum Jülich, 52425 Jülich, Germany
[2] Jülich Aachen Research Alliance (JARA), Fundamentals of Future Information Technology, 52425 Jülich, Germany
[3] Experimentalphysik IV A, RWTH Aachen University, 52074 Aachen, Germany
[4] mProbes GmbH, 52428 Jülich, Germany
[5] Cryovac GmbH & Co KG, 53842 Troisdorf, Germany
[6] Faculty of Mathematics and Natural Sciences, Institute of Physics II, University of Cologne, 50937 Cologne, Germany

[a)] **Current address:** Peter Grünberg Institute (Cryo-Lab), Forschungszentrum Jülich, 52425 Jülich, Germany.
[b)] **Author to whom correspondence should be addressed:** r.temirov@fz-juelich.de

ABSTRACT

We present the design and performance of an ultra-high vacuum scanning tunneling microscope (STM) that uses adiabatic demagnetization of electron magnetic moments for controlling its operating temperature ranging between 30 mK and 1 K with an accuracy of up to 7 μK rms. At the same time, high magnetic fields of up to 8 T can be applied perpendicular to the sample surface. The time available for STM experiments at 50 mK is longer than 20 h, at 100 mK about 40 h. The single-shot adiabatic demagnetization refrigerator can be regenerated automatically within 7 h while keeping the STM temperature below 5 K. The whole setup is located in a vibrationally isolated, electromagnetically shielded laboratory with no mechanical pumping lines penetrating its isolation walls. The 1 K pot of the adiabatic demagnetization refrigeration cryostat can be operated silently for more than 20 days in a single-shot mode using a custom-built high-capacity cryopump. A high degree of vibrational decoupling together with the use of a specially designed minimalistic STM head provides outstanding mechanical stability, demonstrated by the tunneling current noise, STM imaging, and scanning tunneling spectroscopy measurements, all performed on an atomically clean Al(100) surface.

I. INTRODUCTION

Scanning tunneling microscopy (STM) performed in ultra-high vacuum (UHV) at millikelvin (mK) temperatures enables studies of delicate quantum phenomena that occur on surfaces.[1–18] The growing interest in phenomena such as quantum entanglement will most probably boost the demand for mK STM instrumentation. In contrast to STMs operating at higher temperatures, the mK STM technology is much less common. Virtually all of the existing mK STMs share one common feature: They use the technique of ^{3}He–^{4}He dilution refrigeration (DR) to reach base temperatures below 100 mK.[19–31] DR is a powerful technique that combines well with high magnetic fields and UHV conditions, but it also has its shortcomings. Most critically, for the STM operation, DR continuously circulates cryoliquids in the microscope's vicinity, leading to a higher level of mechanical noise. In these circumstances, the search for alternative implementations of the mK STM seems to be well justified.

Here, we describe the design and performance of the first-ever mK STM cooled by adiabatic demagnetization refrigeration (ADR) of electronic spins.[32] Although ADR was the first technique to reach temperatures below 1 K, it has never been applied to STMs, presumably due to the low thermal stability of inorganic salts typically used for ADR. Despite this, our results show that an ADR-based mK STM operating under UHV conditions is feasible and, in some respects, perhaps an even more attractive alternative to the existing approaches. The use of ADR provides several significant advantages: First, ADR works without using helium-3. Second, it enables operation in a mechanically quiet environment due to the omission of any mechanical pumping, which allows the STM to reach very low levels of the tunneling current noise. Third, the solid-state character of ADR-based devices makes the mK STM design very modular, which simplifies its everyday operation and makes the process of its further development much more efficient. The modularity of our setup is embodied in an easily exchangeable millikelvin insert carrying the STM and the paramagnetic pill necessary for ADR. Fourth, ADR enables accurate and fast control of the STM temperature in a wide range without using additional heaters. Finally, the operating time of more than 20 days of the 1 K pot, run in single-shot mode with the high-capacity cryopump, makes any mechanical interventions, besides the refilling of the liquid helium (LHe) dewars, unnecessary and thus makes remote operation of the STM convenient. Although the total consumption of LHe in our setup is about 32 l/day, the hold time is long enough to enable a once-per-week regular refill schedule. Importantly, we recover more than 98% of the consumed helium.

II. SYSTEM LAYOUT

We start presenting our UHV ADR mK STM by describing the system's layout. The aim is to provide a general understanding of the system functionalities rather than to present full details of its technical design. The setup comprises a UHV system, two superinsulated 300 l liquid helium (LHe) dewars, and a removable millikelvin insert (mK stick) on which the STM is mounted (see Fig. 1). One of the LHe dewars hosts the ADR cryostat and the mK stick, while the other one houses a high-capacity cryopump that operates the 1 K pot of the ADR cryostat during the silent regime of the mK STM operation. The whole setup fits inside a vibrationally isolated[33] and electromagnetically shielded[34] laboratory with an area of 5×4 m^2 and a height of 4 m.

A. UHV chamber

The UHV chamber consists of five sections separated by gate valves, as shown in Fig. 1. Below we give a brief description of each section. Preparation chamber 1 (PC1) serves for the UHV sample preparation. It is equipped with a UHV sample manipulator (SM) manufactured by VAb.[35] The SM is used to prepare samples and to transfer them to the STM. The equipment of the PC1 also includes a focused ion gun from Focus GmbH[36] and Auger Electron Spectroscopy-Low Energy Electron Diffraction optics from SPECS.[37] Preparation chamber 2 (PC2) is meant to host more preparation techniques in the future, but at the moment, it is not in use. The base pressure in PC1 and PC2 is typically around 2×10^{-10} mbar.

The cryo-chamber (CC) that hosts the mK stick during STM experiments, as shown in Fig. 1, comprises the ADR cryostat bore and a small chamber inside which the mK stick head is locked and which is positioned directly on top of the cryostat. The CC has three linear motion feedthroughs equipped with pogo-pin contact plates, which establish electrical connections to the mK stick by pressing against the corresponding contact plate of the mK stick head (cf. Fig. 2). The low-voltage wiring necessary for the temperature sensors' readout and control of the heat switches passes through a 51-pin micro SUB-D UHV feedthrough from VACOM.[38] The high-voltage cabling of the STM piezo passes through a separate 15-pin SUB-D UHV feedthrough. Finally, the tunneling current and the bias wires pass through a 4 × SMA coaxial feedthrough purchased from Allectra.[39] The chamber has two additional linear motion stages for operating the mechanisms, which lock (unlock) the mK stick to (from) the manipulator or the cryostat.

The transfer chamber (TC) hosts a custom-designed UHV manipulator for lifting and loading the mK stick (Sec. III B). In addition to the ion- and turbo-pump, the TC is equipped with a non-evaporable getter (NEG) pump from SAES.[40] The TC connects to the CC through a 50 mm long flexible DN100 UHV bellow with a gate valve attached on each side. The mechanical connection between the TC and the CC can be interrupted without disrupting the STM experiment. Having such an option could, in the future, be useful for minimizing electrical or vibrational noise further. More importantly, disconnecting the TC from the CC makes it possible to remove the mK stick out of the UHV without warming up the cryostat. Because the current version of the mK stick is not bakeable (Sec. II D), the pressure in the TC is at the level of 3×10^{-9} mbar.

B. ADR cryostat

The LHe bath cryostat that cools the mK stick to 1 K has been designed and manufactured by CryoVac.[41] The maximum holding time of LHe in the cryostat reaches 14 days. Typically, the 300 l large superinsulated dewar of the ADR cryostat is refilled every seven to ten days. The boil-off rate of LHe from the dewar is about 0.85 l of LHe/h. The relatively high boil-off rate is mainly a consequence of the wide neck of the cryostat, necessary for the magnet setup, compared to its relatively short height, which was intentionally minimized to fit the whole setup in the 4 m high laboratory space. Besides fulfilling the space constraints, the chosen design allows easy access to the magnet and to the 1 K pot in case an intervention is needed by simply extracting the insert from the dewar. An alternative design to minimize the helium consumption would have been possible by replacing the relatively inexpensive superinsulated dewar with a custom-designed cryostat. This, however, would only come at the cost of losing the above mentioned flexibility.

The system of superconducting magnets installed in the ADR cryostat was custom-designed by Cryomagnetics.[42] It consists of a pair of superconducting coils stacked axially on top of each other, as shown schematically in Fig. 1. The lower coil with a maximum field of 8 T performs the ADR, while the upper 8 T coil generates the B field in the sample region. The ADR magnet provides the necessary field homogeneity in the ADR pill region. The sample magnet has a set of compensating coils that reduce its stray field in the ADR magnet region below 5 mT at the maximum field of 8 T.

The inner bore of the cryostat comprises a 50 mm wide stainless steel tube, which at the same time is the inner wall of the CC,

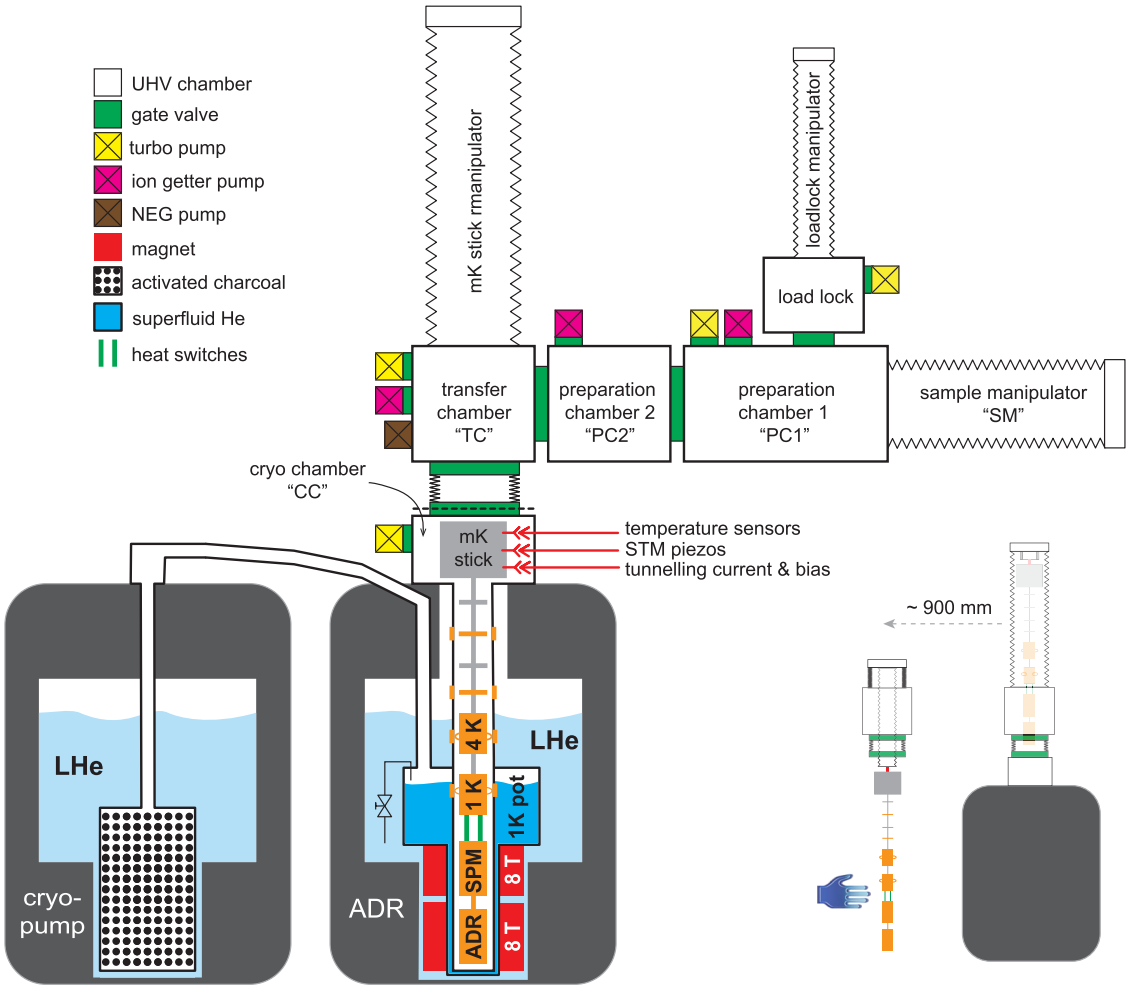

FIG. 1. Schematic layout of the mK STM setup comprising the UHV chambers, the ADR cryostat hosting the mK stick, and the high-capacity cryopump. The main UHV system, which includes the load-lock, preparation chambers 1 and 2, and transfer chamber, connects to the cryostat via a flexible bellow. To extract the mK stick out of the vacuum, the cryostat and the UHV system must be separated at the plane marked by the dashed line. Bottom right: the inset shows the extraction of the mK stick out of UHV. The frame supporting the UHV system is translated sideways in the direction perpendicular to the plane of the main figure for the extraction.

interrupted at specific heights by four gold plated copper rings (see Fig. 1). These copper rings serve as thermal coupling of the mK stick to the cryostat. The upper two rings contact the two mK stick copper baffles (see Fig. 2). The lower two rings thermalize the 4 and 1 K stages, respectively, of the mK stick.

The lowest copper ring thermalizing the 1 K stage is a part of the outer wall of the 1 K pot. The 1 K pot with a volume of 1.3 l receives LHe from the dewar of the bath cryostat via a capillary line, as illustrated in Fig. 1. The line is equipped with a needle valve for the regulation of the LHe flow. The 1 K pot is thermally isolated by the surrounding inner vacuum chamber (IVC) (not shown in Fig. 1 to avoid clutter). When the supply capillary is closed, the 1 K pot enters the single-shot mode, reaching a minimal temperature of 0.975 K. The 1 K pot was designed to operate at least for two weeks under a load of up to 3 mW. In practice, the operation time of the 1 K pot is about 25 days in the single-shot mode without interruption, indicating a much smaller thermal load in our setup.

C. High-capacity sorption pump

The high-capacity cryopump was also designed and manufactured by CryoVac[41] and uses activated charcoal as the sorption material.[43] Sorption pumps have been extensively used for ^{3}He and ^{4}He cryogenics for more than half a century,[44] allowing miniaturization of sub-Kelvin coolers.[45] The capacity of our sorption pump as well as its external mode of operation makes it suitable for any pumped helium stage that is usually operated with a mechanical pump without any modification of the cryogenic setup. The room temperature part of the pumping line that connects the cryopump to the 1 K Pot exhaust is made with a 1.5 m long KF 50 bellow. The cryopump

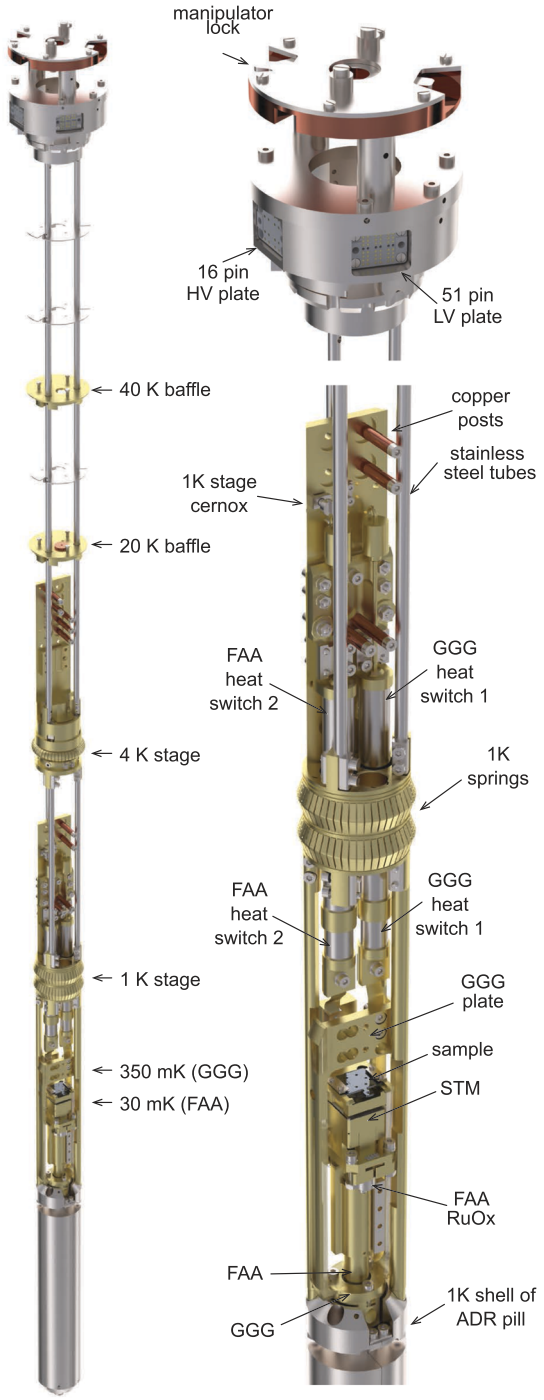

FIG. 2. Rendered CAD model of the mK stick. Left: mK stick in its full length of 156.5 cm. The arrows indicate locations of different temperature stages. Top right: head of the mK stick with the mechanism locking it to the vertical manipulator that loads it into the cryostat. Two of the contact plates used for establishing the electrical contacts to the temperature sensors and the STM piezo are also visible. The third contact plate establishing the coaxial bias and tunneling current contacts is located on the back side. Bottom right: image detail of the mK stick below the 4 K stage without wiring. For further information, see text.

capacity was designed to provide more than two weeks of uninterrupted operation of the 1 K pot of the ADR cryostat under a heat load of 3 mW. It operates steadily for about a month in real conditions, after which it can be fully regenerated within 3 h. The sorption pump is surrounded by an evacuated volume (not shown in Fig. 1 to avoid clutter) that can be filled with LHe from the main LHe bath through a needle valve. When evacuated, this volume provides thermal insulation from the LHe bath and allows the regeneration of the pump by heating it to 40 K and pumping the desorbing helium gas with a scroll pump. The boil-off rate of the superinsulated LHe dewar of the cryopump is about 0.5 l LHe/h, which results in a maximum holding time of three weeks. We typically refill the cryopump dewar once in 14–20 days.

D. mK stick

The mK stick is a crucial part of the mK STM, as it hosts both the STM and the paramagnetic pill (ADR pill) necessary for reaching millikelvin temperatures. As noted above, the mK stick has no permanent electrical or mechanical connections to the rest of the setup. Therefore, it can be quickly extracted out of UHV and even exchanged without warming up the ADR cryostat. This feature allows for a unique degree of modularity of our setup.

The mK stick comprises the following essential parts (cf. Fig. 2): the head featuring electrical contact plates and the locking mechanism for attaching the mK stick either to the manipulator or to the top of the cryostat; three thin-walled stainless steel tubes forming the structural backbone of the mK stick down to its 1 K stage, below which the structure is supported by three gold plated copper rods; three stainless steel baffles for radiation protection; two copper baffles thermalized to the 40 and 20 K copper rings of the CC (Sec. II B); the 4 K stage with the gold plated CuBe spring establishing the thermal contact to the 4 K copper ring of the CC; the 1 K stage with the two gold plated CuBe springs coupling it thermally to the 1 K pot; two ^{3}He gas-gap heat switches (HSs), designed and manufactured by Chase Research Cryogenics;[46] a home-built STM; and finally a two-stage ADR pill, designed and manufactured by Entropy[47] and attached to the very bottom of the mK stick.

For monitoring the mK stick temperature, we use four temperature sensors: two calibrated Cernox sensors (Lakeshore)[48] are mounted at the 1 and 4 K stages, respectively, and two calibrated RuOx sensors from Entropy[47] monitor the temperature of the two stages of the ADR pill (see below). The sensor wiring running between 300 and 1 K is made of a twelve-twisted-pair constantan ribbon from CMR.[49] Below the 1 K stage, the wiring continues with three individual four-twisted-pair NbTi ribbons acquired from CMR.

For the wiring of the STM, we use a shielded twisted-pair cable obtained from GVL Cryogenics.[50] This cable has a braided constantan shield with a resistance of 6 Ω/m, while the 0.1 mm diameter inner brass conductors have a resistance of 8 Ω/m. The inner conductors are varnished and covered with Teflon for additional electric isolation. We have tested the cables in UHV and detected no appreciable outgassing at the highest tested temperature of 150 °C.

Due to its construction, the piezo-system of our home-built STM (Sec. II E) needs only five electrical connections for its

operation. These are implemented with three shielded twisted-pair lines. The wiring of the STM bias and the tunneling current consists of two twisted-pair lines in which we turned the two inner conductors of the pair into one by soldering them together at both ends. All twisted-pair cables run from 300 K down to 30 mK without physical interruption. Each cable is wrapped around two copper posts for thermalization: one located at the 4 K and the other at the 1 K stage (Fig. 2). Furthermore, we thermalize these cables by pushing them into 5–15 cm long, 3 mm deep, and 0.8 mm wide groves in the copper bodies of both the 350 and the 30 mK plates of the mK stick. The last few centimeters of the bias and the tunneling current wires consist of unshielded NbTi superconducting wire to improve thermal decoupling and additionally block high-frequency noise.[27]

The bottom of the mK stick features a commercially acquired ADR pill that contains two paramagnetic materials: ferric ammonium alum (FAA) with the chemical formula $NH_4Fe(SO_4)_2 \cdot 12H_2O$ and gadolinium gallium garnet (GGG)—$Gd_3Ga_5O_{12}$. Figure 3 reveals the principal scheme of the ADR pill, which consists of three thermally decoupled stages. The outer aluminum shell is in good thermal contact with the 1 K stage of the mK stick. It encloses the second shell made of gold plated copper with a 201 g single crystal of GGG firmly attached to it. This assembly that we refer to as the GGG stage reaches 350 mK during the ADR cooling cycle (Sec. III C). As mentioned above, the GGG stage provides precooling for the wiring that passes to the STM and simultaneously reduces the heat leak from the 1 K stage toward the FAA stage of the ADR pill that reaches the lowest temperature. The GGG stage is also attached to one of the two gas-gap heat switches (cf. Fig. 2 and Sec. III C) that connects it to the 1 K stage of the mK stick. A calibrated RuOx sensor fixed to the GGG stage provides the reading referred to as "GGG temperature" or T_{GGG}.

The core of the ADR pill—the FAA stage—that reaches the lowest temperature of 26 mK comprises crystalline FAA with a mass of 210 g enclosed in a UHV-tight stainless steel container. The FAA crystal is in good thermal contact with a thick copper rod that sticks out of the container and provides thermalization for the STM and the second RuOx sensor, the reading of which is then referred to as FAA temperature or T_{FAA}. The FAA stage of the ADR pill is also connected to the 1 K stage of the mK stick through its own gas-gap heat switch (cf. Fig. 2 and Sec. III C).

One final note on the temperature stability of the ADR pill is due. Unlike the GGG crystal that is thermally stable, the FAA crystal contains water and its melting temperature is about 40 °C.[51] This makes the ADR pill and the whole mK stick not-bakeable. As will be demonstrated below, this technical complication does not prevent us from preparing and working with atomically clean sample surfaces. At the same time, we are also developing a new type of bakeable ADR pill using novel, thermally stable magnetocaloric materials.[52]

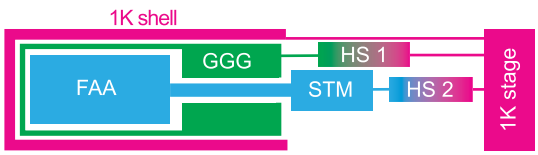

FIG. 3. Principal scheme of thermal flow in the ADR pill. Two gas-gap heat switches (HS) connect the FAA and GGG stages to the 1 K stage. In the "OFF" state of the heat switches, the FAA and GGG stages decouple thermally from the 1 K stage. The FAA and GGG stages are also thermally isolated from each other. The STM is firmly screwed to the FAA stage. The 1 K shell of the ADR pill is permanently well-connected to the 1 K stage of the mK stick.

E. STM

A unique feature of our home-built STM (cf. Fig. 4) is that both *z*-coarse and *xyz*-scanning functions are implemented in a single piezoceramic tube. Such a design makes the STM very compact and thus less sensitive to mechanical noise. It also needs fewer high-voltage lines for its operation, thus also reducing the thermal load on the mK stick. As shown in the right panel of Fig. 4, the *z*-coarse approach motor of our STM exploits the slip-stick mechanism: A tungsten rod, held by two CuBe springs inside a CuBe tube, which is firmly attached to the upper end of the piezo-tube, can be accelerated slowly in the direction of the long axis of the tube by extending (contracting) the piezo. The tungsten rod makes a coarse *z* step when the extension (contraction) of the piezo-tube reverses rapidly, causing a high acceleration of the rod that eventually overcomes its friction with the springs. The voltage pulse used to produce a single coarse step toward the surface is shown in Fig. 5(a). The pulse is applied to the inner contact of the piezo-tube against all its four outer contacts. To move in the opposite direction, the time profile of the pulse is inverted. The coarse steps are made with the piezo in its fully contracted state (i.e., under high positive voltage), which is necessary for the subsequent test of the tunneling contact after the coarse step during auto-approach. The pulse sequence used for the auto-approach is shown in Fig. 5(b).

The STM fine scanner is operated conventionally by applying voltages of opposite polarity to the corresponding pairs of *x* and *y* electrodes. For fine scanning of *z*, the inner contact of the

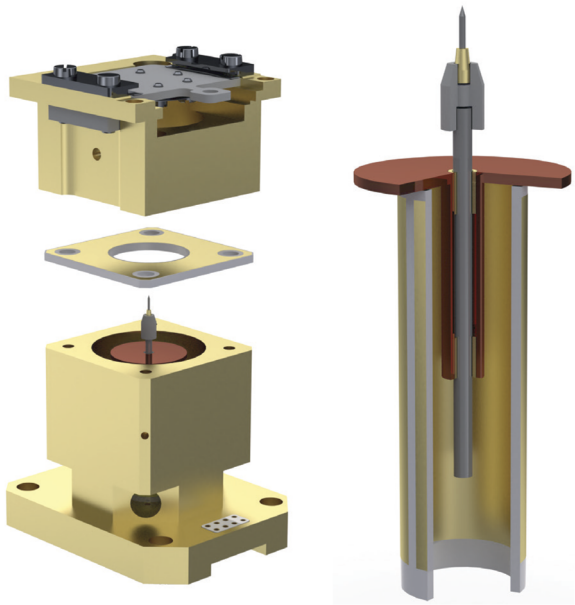

FIG. 4. Left: exploded view of the home-built STM. The top part of the STM is electrically isolated from the STM body by a sapphire plate. The STM body hosts a single piezo-tube used for both the coarse and fine motion of the STM tip. Right: cut view of the piezo-tube, revealing the stick slip coarse motor (see text for details).

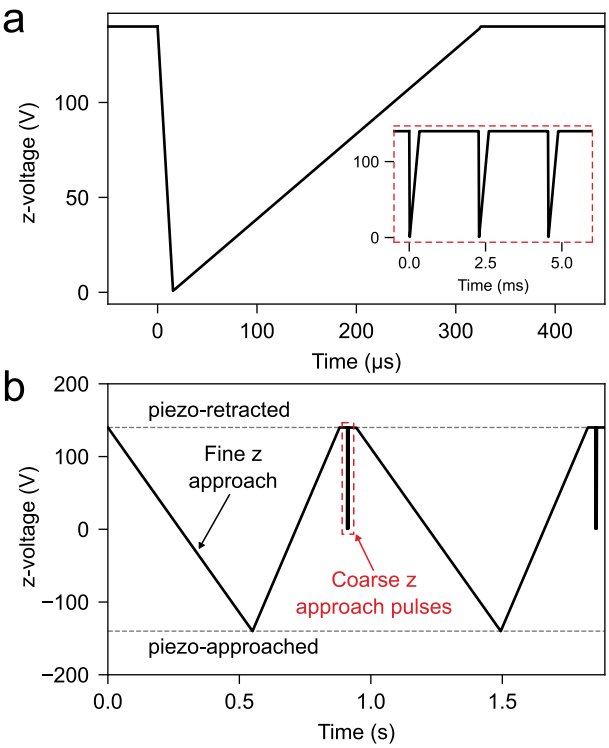

FIG. 5. (a) A voltage pulse producing a single coarse *z* step toward the surface. When inverted in time, the pulse produces a single step away from the surface. Inset: a sequence of three coarse *z* pulses typically employed during auto-approach. (b) A voltage pulse sequence applied during the auto-approach.

piezo-tube is biased against all four outer contacts. Operating with voltages of up to 150 V, we can scan an area of 2.5 × 2.5 μm^2 at the lowest millikelvin temperatures. It should be possible to reach a 6.5 × 6.5 μm^2 scan range by applying voltages of up to 400 V.

Our STM accepts standard flag-type sample plates. The sample is inserted into the top part of the STM, electrically isolated from the rest of the STM body by a 1 mm thick sapphire plate covered from both sides with a thin film of gold to improve thermal contact.

III. SYSTEM OPERATION AND CHARACTERISTICS

A. Initial cooldown

The initial cooldown of the ADR cryostat starts with precooling it to liquid nitrogen (LN2) temperature. Figure 6 shows that the cooling of the mK stick from room temperature to 80 K takes about 24 h. During this time, the IVC is kept at a pressure of few millibars of helium gas. After reaching the desired temperature and blowing LN2 out of the superinsulated dewar, the filling with LHe starts. When the temperature of the 1 K stage reaches 40 K, the IVC has to be evacuated, and briefly afterward, the pumping of the 1 K pot with a mechanical pump starts. As shown in Fig. 6, after about 35 h, the temperature of the 1 K stage drops below 2 K. The cooldown of the cryopump proceeds analogously and is not described here in detail. The final temperatures of the 4 and 1 K stages of the mK stick reached in different regimes of the ADR cryostat's operation are listed in Table I.

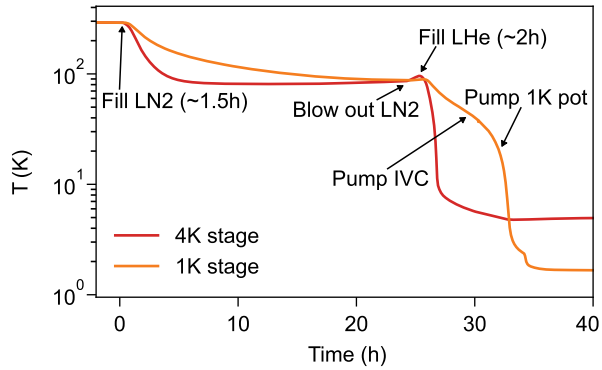

FIG. 6. Evolution of the 4 K stage and 1 K stage temperatures of the mK stick during the initial cooldown from 300 K. For further information, see text.

B. mK stick manipulation

Our mK STM is designed for full operation in laboratory rooms with a minimal height of only 4 m. This required the design and manufacture of a special manipulator for *in situ* sample exchange and the extraction of the mK stick from the bath cryostat. The manipulator is motorized and operated with the help of custom-made software. A typical mK stick manipulation cycle that is performed to load the sample into the STM (or remove it from the STM) is exhibited in Fig. 7.

In the initial position [Fig. 7(a)], both the outer and inner bellows of the manipulator are in the contracted state and the stick resides in the STM measurement position (inside the CC), while all the electrical contacts to the mK stick are disengaged, i.e., all corresponding linear stages in the CC (Fig. 1) are in the retracted position. Next, a push–pull rod is attached to the bottom of the inner bellow [Fig. 7(a)], and the bellow is expanded downward until it reaches the head of the mK stick [Fig. 7(b)]. Then, the head of the mK stick is fixed to the manipulator by actuating the lock situated in the upper part of the mK stick (Fig. 2), and the manipulator lifts the mK stick [Fig. 7(c)] by contracting the inner bellow to its original state. Here, the push–pull rod is removed, and the outer bellow of the manipulator is expanded, lifting the mK stick [Fig. 7(d)] to the position at which the sample can be loaded into (or extracted from) the STM using the sample manipulator (SM) (see Fig. 1 and Sec. II A). The

TABLE I. Temperatures of the different stages of the mK stick depending on the state of the heat switches. The 1 K pot is operated in single-shot mode. Note that the temperature of the 4 K stage varies with the LHe level of the ADR cryostat. Also note that turning the heat switches on raises the temperature of the FAA, GGG, and 1 K stages because the two 10 kΩ (room temperature value) resistors that are used to warm up the charcoal inside the heat switches (see Sec. III C) dissipate about 0.36 mW of power each when biased by 2 V.

	Heat switches on (K)	Heat switches off (K)
4 K stage	4.55–5.10	4.55–5.10
1 K stage	1.70	1.03
GGG stage	1.66	1.02
FAA stage	1.68	1.03
1 K pot	1.04	0.98

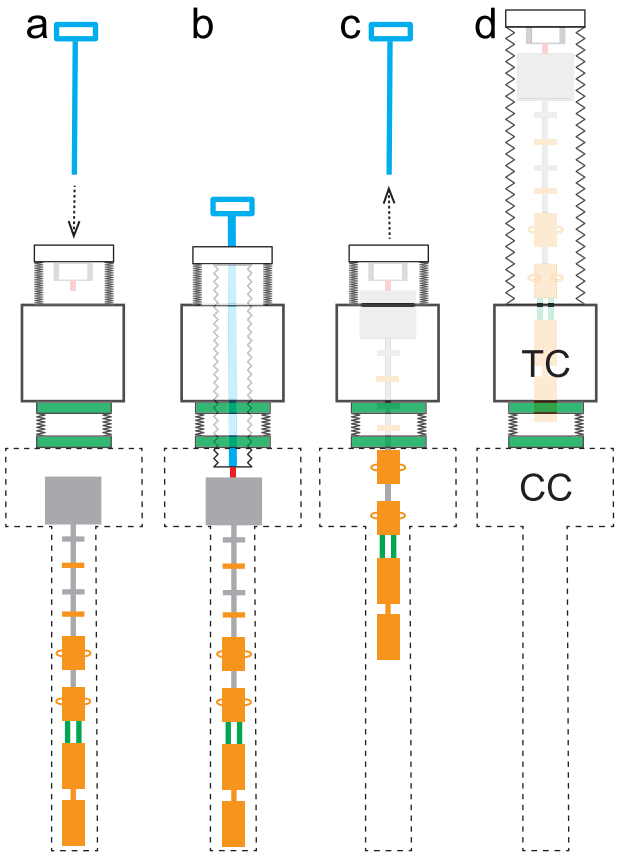

FIG. 7. (a)–(d) The sequence of manipulation steps used to remove the mK stick from the ADR cryostat. To remove the mK stick from the vacuum, the manipulation continues with the sequence (d)–(a), executed after the vacuum connection between TC and CC is broken, TC is vented, and the UHV chamber frame shifted to the side by ~900 mm, which clears the space below the manipulator. The dashed line shows the contour of CC. For further information, see text and the inset of Fig. 1.

combined action of the outer and inner bellows allows for a vertical travel distance of the mK stick that exceeds the elongation of the manipulator itself.

After extracting or loading the sample, the mK stick is loaded back by the reversed manipulation sequence. Figure 8 shows that the full manipulation cycle, i.e., lifting the mK stick, extracting or loading the sample, and loading the mK stick back into the cryostat, takes about 30–40 min. During this time, the 1 and 4 K stages of the mK stick warm up to 40 and 60 K correspondingly. A subsequent cooldown of both stages back to 4 K takes about 4–5 h.

Note that during the manipulation procedure, the temperatures of the different stages of the mK stick cannot be read out. The temperature readings of the Cernox thermometers of the 4 and 1 K stages become available immediately after the stick is loaded back into the cryostat. Since the RuOx sensors of the GGG and FAA stages are only calibrated up to 5.9 and 7.6 K, respectively, their temperature readings become available only when the corresponding temperatures are reached on these stages. From the temperature reading of the 1 K stage after finishing the manipulation sequence,

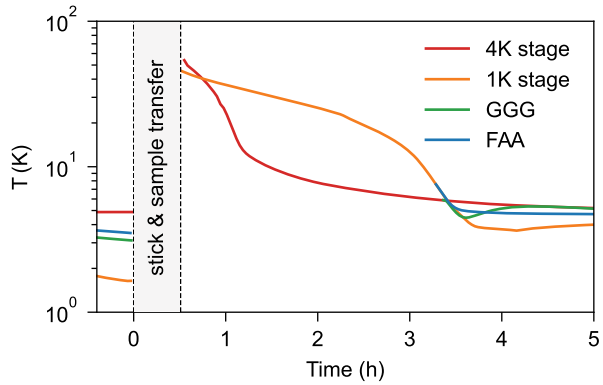

FIG. 8. The temperature evolution of the different stages of the mK stick after a sample transfer. During the sample transfer, the horizontal sample manipulator is cooled by LN2.

we expect that the sample temperature also remains below 40–50 K in the lifted state of the stick, making the deposition of individual atoms and molecules onto the sample surface possible.

The extraction of the mK stick out of UHV starts with lifting the mK stick up from the cryostat, i.e., executing the steps shown in Fig. 7. After reaching the stage shown in Fig. 7(d), the gate valve to the CC is closed, and the TC is disconnected from the CC and vented. Then, the frame supporting the UHV system (PC1, PC2, and TC) is moved relative to the CC in the direction perpendicular to the plane of Fig. 1 by a distance of 900 mm (see the inset of Fig. 1). After this translation, the space below the TC is free and the manipulator is brought back to the state shown in Fig. 7(b) so that the mK stick can be removed manually from it, as shown in the inset of Fig. 1.

C. ADR cycle

The ADR technique is well-established, and its detailed description can be found in numerous literature sources.[32] Here, we give a brief account of it, noting that the cooling is possible due to the magnetocaloric effect in certain paramagnetic materials that possess a large magnetic entropy at low temperatures. Assuming FAA to be a collection of noninteracting magnetic dipoles, one obtains the dependence of its magnetic entropy on the temperature T and the external field B[53] as

$$S(B,T) = nR\left\{x(\coth(x) - y\coth(xy)) + \ln\left(\frac{\sinh(xy)}{\sinh(x)}\right)\right\}, \quad (1)$$

with $x = \frac{\mu_B g B}{2k_B T}$ and $y = 2J + 1$. Here, n is the number of moles of FAA in the ADR pill, R is the ideal gas constant, μ_B is the Bohr magneton, g is the g-factor of an electron, k_B is the Boltzmann constant, and $J = 5/2$ is the total angular momentum of the paramagnetic ions in FAA.[53]

Figure 9(a) shows plots of $S(B,T)$ calculated with Eq. (1). The ADR cooling cycle starts at a fixed temperature and zero B field (point 1). In the first step, the B field is increased to a maximum (6 T in our case) while keeping the paramagnetic material in isothermal contact with its environment (point 2). The increase in the field leads to a drop in the magnetic entropy of the paramagnetic material. At

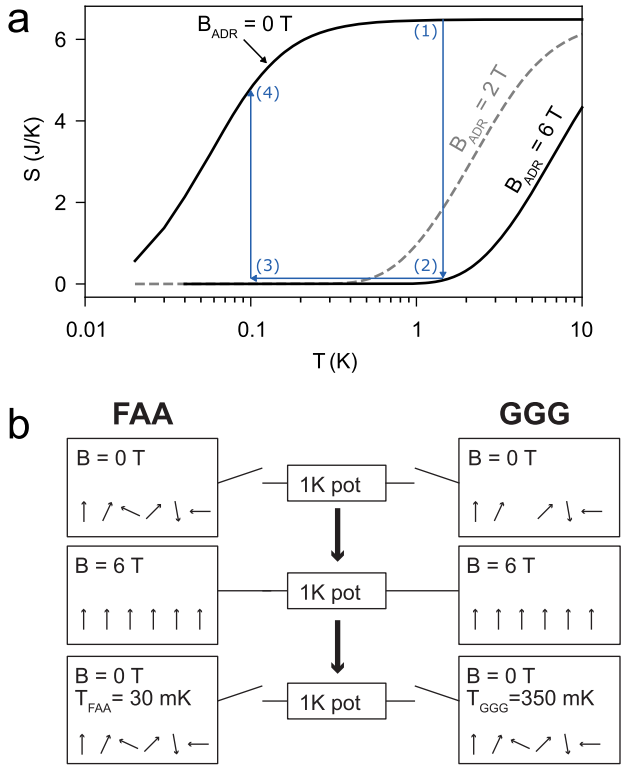

FIG. 9. (a) $S(B, T)$ of an FAA crystal with a mass of 210 g calculated using the non-interacting dipole model.[53] The trace (1)–(4) indicates a possible ADR cooling cycle in which the isothermal magnetization (1)–(2) is performed at 1.5 K, and the adiabatic demagnetization (2)–(3) is stopped at 0.1 K, after which the remaining entropy is used to keep the temperature constant (3)–(4). (b) Technical scheme of the two-stage ADR pill employed in our cryostat.

the same time, its thermal entropy initially rises because the heat corresponding to the magnetic entropy before magnetization remains present. However, since the paramagnetic material is in contact with the thermal reservoir of the environment, this heat is transported away (isothermal conditions). In the second step, the paramagnetic material and that part of the environment that is to be refrigerated are decoupled from the thermal reservoir. In this adiabatic condition, the B field is then decreased to zero. While the total entropy remains constant (adiabatic condition), there is a transfer from thermal to magnetic entropy as the magnetic moments overcome the alignment in the B field. This heat transfer leads to a drop in temperature. The ADR base temperature that can be achieved in this way is defined by two parameters: the starting temperature in point 1 and the maximum field value in point 2. Note that the magnetic ordering temperature of FAA defines the absolute lower boundary of temperatures that are attainable by ADR with FAA. Of course, also the heat capacity of the load to be cooled has an effect on the effective base temperature. However, this is usually much smaller than the heat capacity of the system of paramagnetic moments because the specific heat of FAA in the relevant range of temperatures is much larger than that of, e.g., copper.[32,54]

Alternatively, stopping the demagnetization at a target temperature before the B field reaches zero (point 3) allows one to hold this temperature constant by slowly decreasing the B field such that the increase in the magnetic entropy of FAA balances the residual heat flux from the thermal reservoir into the decoupled system (FAA plus load to be cooled). Clearly, the temperature regulation becomes impossible when the B filed reaches zero. The holding time depends on the magnetic entropy of the FAA at the given temperature and the heat leak $\dot{Q}$ (for more details, see Sec. III D).

To establish adiabatic conditions in the mK stick, we employ two commercially acquired UHV-compatible gas-gap heat switches (Fig. 2). Here, we show the procedure schematically in Fig. 9(b). A gas-gap heat switch typically comprises a thin-walled stainless steel tube containing ^{3}He at a pressure of a few mbar and a miniature charcoal pump attached to it. The principle of its operation has been described in detail in the literature.[55] Briefly, heating the charcoal in the switches to about 15–20 K increases their thermal conductivity to 10–50 mW/K, thereby establishing a thermal connection between the 1 K pot and both stages (FAA and GGG) of the ADR pill. With the heat switches in this ON state, the ADR magnet is ramped up to 6 T. The 1 K pot bath removes the heat generated during the magnetization (magnetic entropy is transferred in thermal entropy). When T_{FAA} and T_{GGG} approach the 1 K pot temperature, the heat switches are turned to their OFF state by deactivating the heating of the charcoal. The ^{3}He pressure inside the switches decreases, reducing the heat conductivity to ~1 μW/K (per switch). When the FAA and GGG stages decouple from the 1 K pot bath, the final step of demagnetization may start.

Figure 10 shows an actual ADR run that starts with turning on the pumping of the 1 K pot. As becomes apparent from Fig. 10(b), the whole system needs about 2 h to reach the base temperature near 1 K (see Table I). The following ramp up of the ADR magnet proceeds with the rate of 1.2 mT/s in order to keep the temperature of the FAA and GGG stages below 5 K. After reaching the maximum field, it takes about 3.5 h until the temperature of the ADR pill drops again to 1.6 K. Next, the GGG heat switch is turned off. Turning off the FAA heat switch with a delay of 0.5 h results in a decrease in the FAA temperature further to 1.4 K because the power dissipated by the heaters of the charcoal in the heat switches is only as half as large when only one switch remains in the ON state (see Fig. 10). With both heat switches in the OFF state, the ADR magnet is demagnetized with the rate of 1.2 mT/s. This relatively slow demagnetization prevents the generation of excessive heat by eddy currents. However, our experience shows that the demagnetization rate can be increased to at least 2–3 mT/s without noticeable deterioration of the thermal performance.

The demagnetization results in a decrease in the temperature of the ADR pill. The GGG temperature reaches 350 mK when the field of the ADR magnet is about 1 T. At these conditions, GGG experiences an antiferromagnetic ordering transition[56] that precludes further cooling. In contrast, the FAA temperature keeps dropping further and reaches a minimum of 26.8 mK, close to which temperature the electron spins inside FAA also order.[54] This point marks the end of the ADR cycle. After reaching its lowest temperature, the ADR setup starts warming up because of the residual heat leak. Figure 10(c) shows that it takes T_{FAA} about 15 h to reach 50 mK and more than 25 h to 100 mK. After the warming up, the ADR pill needs to be regenerated by repeating the cycle. In our setup, the described

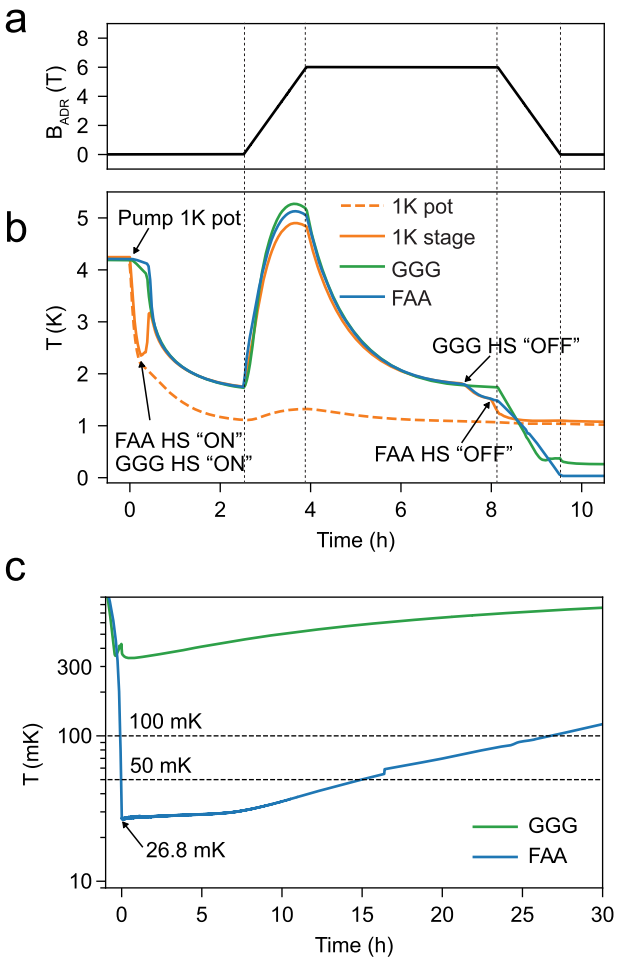

FIG. 10. (a) and (b) Typical cooling cycle starting from 4.2 K and finishing at the lowest attainable millikelvin temperature. (a) Changes of the *B* field of the ADR magnet during the ADR cycle and corresponding to the temperature profiles displayed in (b). Changes in *B* influence the temperature: During magnetization, the temperatures increase. After reaching the maximum value, *B* is kept constant to allow for thermalization of the ADR pill. Demagnetization starts when T_{FAA} = 1.52 K and T_{GGG} = 1.78 K. The lowest temperature is reached when B_{ADR} = 0 after which T_{FAA} and T_{GGG} start increasing. (c) Evolution of the T_{FAA} and T_{GGG} after the end of the ADR cycle shown in (a) and (b).

ADR cooling cycle is fully automated and performed without any human intervention.

D. Temperature regulation

One of the unique features of ADR is the possibility to precisely control the temperature via regulating the *B* field. We establish such a control by introducing a software feedback loop that receives an input from the FAA temperature sensor and responds by regulating the current that flows through the ADR magnet's coil. As shown in Fig. 11, within several minutes, the regulation achieves a 7 μK accuracy in stabilizing a desired temperature in the lower millikelvin range. Notably, regulation works well also at higher temperatures, albeit with a somewhat smaller accuracy.

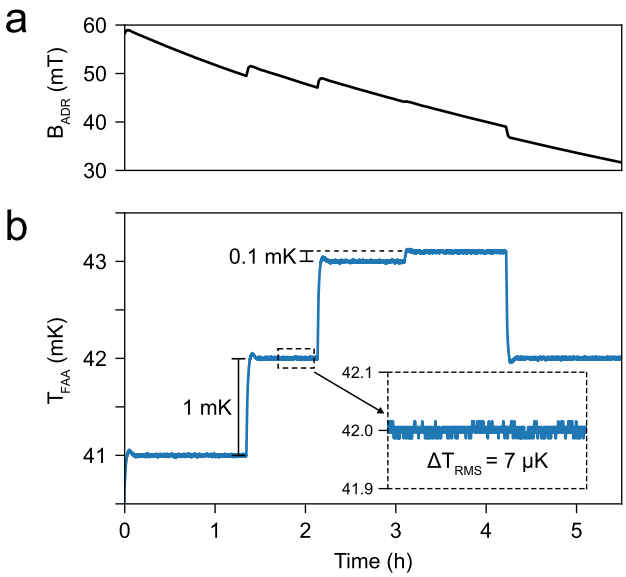

FIG. 11. Temperature regulation with ADR. (a) The *B* field of the ADR magnet as set by the software feedback loop to execute the temperature trace shown in (b). (b) An exemplary trace of the T_{FAA} realized by the ADR regulation. The inset shows the magnification of a constant temperature segment to visualize the temperature regulation accuracy.

Using the temperature regulation technique, we also evaluate the residual heat leak toward the FAA stage from the environment. Setting the temperature to 40 mK immediately after finishing the demagnetization cycle, we measure the FAA's holding time at this temperature. As shown in Fig. 12, the holding time equals 15 h. Applying the analytical formula for $S(B,T)$ for FAA, we obtain the heat leak $\dot{Q} = TdS/dt \approx 4$ μW from the experimental $B(t)$ data. Recalling that the expected heat leak of the FAA heat switch should be about 1 μW, we conclude that the STM and RuOx sensor wiring plus the FAA stage's thermal isolation inside the ADR pill introduce an additional heat leak of 3 μW.

Calculating the total heat $Q(T_3)$ that can be absorbed by the FAA stage of the ADR pill at the temperature T_3 (point 3 in Fig. 9) as $Q(T_3) = T_3 * (S(0,T_3) - S(B_{max},T_2))$[53] and using the obtained value of the heat leak, we predict the holding time of our FAA stage at different temperatures. As Fig. 12 shows, the calculated values agree well with the experimentally measured holding time data. The model curve also shows that the holding time at 100 mK may be as long as two days.

The ADR magnet has no compensation coils to reduce its stray field in the sample region. The stray field produced by the ADR magnet at the position of the sample is about 20 times smaller than the maximum field of the ADR magnet. Accordingly, a variation of ~5 mT/h of the ADR magnet field during temperature regulation (see Figs. 11 and 12) would result in a ~0.25 mT/h change in the sample region. Note, however, that this stray field can, in principle, be fully compensated by the field of the sample magnet. When the ADR magnet is not used for temperature regulation, there are no additional stray fields in the sample region.

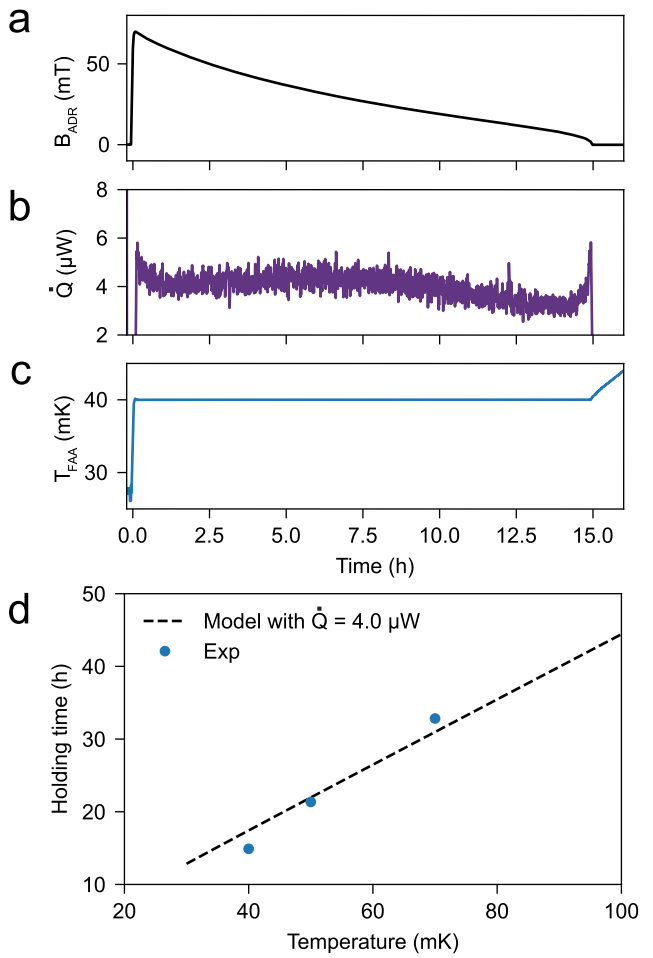

FIG. 12. (a) Evolution of the *B* field produced in the ADR magnet by the software feedback loop for holding T_{FAA} = 40 mK. The regulation starts at the end of the ADR cooling cycle, i.e., after the ADR magnet field has reached zero and the FAA temperature has reached 27 mK. To increase the temperature to 40 mK, a *B* field of 70 mT is initially applied. The regulation ends when the ADR *B* field reaches zero again. Note that the regulation at $T > 40$ mK at this point remains still possible. (b) The heat leak to the FAA stage at $T = 40$ mK, extracted using the data in (a). (c) T_{FAA} resulting from the regulation shown in (a). (d) Holding times measured at specific temperatures. Each experimental point was measured by initiating the temperature regulation immediately after the ADR cooling cycle, similar to (a). The dashed line is calculated with the assumption of a heat leak to the FAA stage of 4 μW. For details, see text.

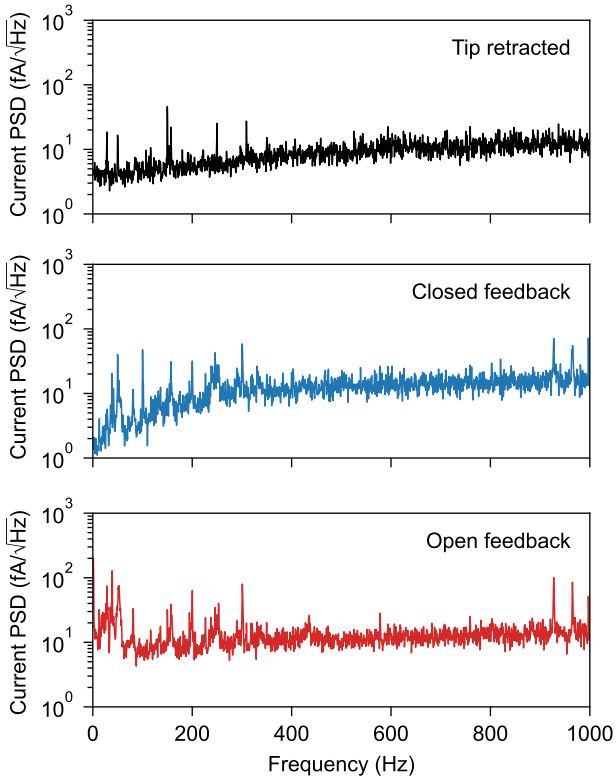

FIG. 13. Power spectral density of the tunneling current I_T acquired at T_{FAA} = 29 mK at three different conditions: tip retracted, closed feedback, and open feedback. The data were taken with a PtIr tip on a clean Al(100) surface. The spectra in contact were acquired at a setpoint I_T = 100 pA and V = 10 mV.

E. STM performance

We demonstrate the STM performance by first showing in Fig. 13 the power spectral density of the tunneling current measured at 29 mK over an atomically clean Al(100) surface prepared in UHV by repeated cycles of Ar^+ sputtering and annealing at 500 °C. The tunneling current was measured using a fixed 10^9 gain amplifier from NF Corporation[57] at a setpoint of I_T = 100 pA and V = 10 mV. The noise data as well as the STM images and dI/dV spectra were acquired with Nanonis SPM control electronics.[58] The spectra in Fig. 13 show that our system reaches a remarkable degree of mechanical stability. The high stability of our STM junction also results in topographic noise smaller than 0.5 pm (peak to peak), as the scanned image of the Al(100) surface demonstrates (Fig. 14). Finally, neither the warming up of the STM after finishing an ADR cooling cycle nor the ADR regulation of the temperature affects the STM noise.

Both the vertical and lateral drift of the STM junction settle at about 30 pm/h in less than 2–3 h after finishing an ADR cooling cycle. It is enough to withdraw the tip by roughly 50 nm to prevent it from crashing into the surface during the cooling cycle. Besides that, the total lateral drift of the tip caused by the ADR cooling cycle is only about ~100 Å. In a similar manner, the STM junction and the nanoscale working area are left intact also when refilling LHe, which thus enables us to perform STM experiments with the same tip on the same nanostructure virtually forever.

With respect to the STM performance in magnetic field, our preliminary tests show no noticeable deterioration when the sample magnet is operated in the persistent mode. Additionally, ramping the sample coil with the speeds of up to 4 mT/s, we did not have any difficulty in sustaining a stable tunneling contact between the STM tip and the surface.

F. STM junction effective temperature

It has become a common practice to demonstrate the effective electronic temperature of the mK STM junction by measuring the

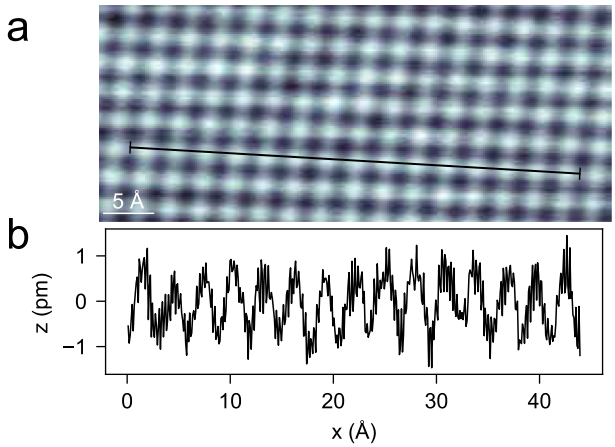

FIG. 14. Top: unprocessed constant current STM image of a clean Al(100) surface scanned at T_{FAA} = 196 mK with a clean PtIr tip. The image, exhibiting the atomic structure of the surface, has a resolution of 512 pixel/line and was scanned with a speed of 8.1 nm/s. The tunneling setpoint was I_T = 2 nA and V = 1 mV. Bottom: a profile along the black line shown in the image.

density of states around a superconducting gap. Such a measurement is necessary because the phonon bath's temperature, measured in our case by the RuOx sensor, may not reflect the electronic temperature. Therefore, we present a scanning tunneling spectroscopy (STS) measurement of the superconducting gap of the Al(100) surface. Figure 15 displays a single dI/dV spectrum (raw data) acquired with the help of the internal lock-in of the Nanonis controller electronics.[58] We filtered the bias and all five high-voltage lines to the STM piezo to minimize the electric noise. The bias line was filtered with a commercial 5000 pF pi-filter[59] mounted in line with a 3 kΩ resistor, while for the high-voltage lines, we used 4500 pF pi-filters.[60] As one can see in Fig. 15, the Maki fit[24,28] of the spectrum comprising the gap and the coherence peaks yields the effective temperature T_{eff} = 157 mK. Although the obtained value is higher than the

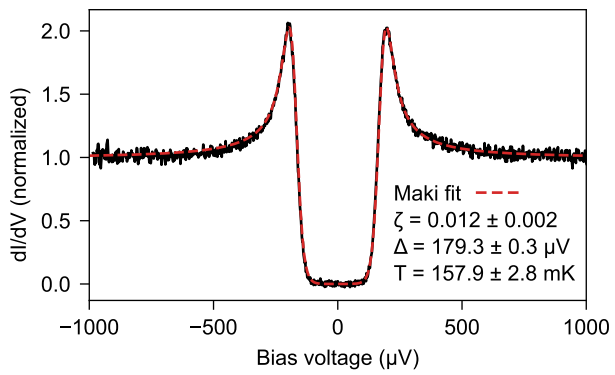

FIG. 15. Measurement of the differential tunneling conductance dI/dV on Al(100) at T_{FAA} = 27.5 mK using a clean PtIr tip (black curve). The single dI/dV spectrum (raw data) is measured by the lock-in technique with an AC modulation amplitude of 4 μV and a frequency of 187.7 Hz using a 1/100 bias voltage divider. The acquisition time was 189 s (1024 data points with 150 ms integration time). The tip was stabilized at I_T = 500 pA and V = 1 mV. The red dashed curve shows the fit based on the Maki function.[24,28]

(phonon bath) temperature of 27.5 mK at which the measurement has been performed, it is within the range of the values reported for the DR-based mK STMs.[22–30]

Surprisingly, however, we find that the electric noise filtering scheme does not substantially affect T_{eff} in our case. Removing the bias line filter increases T_{eff} to 225 mK. Grounding the temperature sensor wiring does not affect T_{eff} at all. At the same time, in agreement with Ref. 31, we see that the type of the current amplifier used for STS influences T_{eff}: Switching to a Femto DLPCA 200[61] increased T_{eff} to 200 mK.

IV. CONCLUSION AND OUTLOOK

In conclusion, we have built—to the best of our knowledge—the first UHV STM that uses adiabatic demagnetization of electronic spins to perform measurements at well-controlled millikelvin temperatures. Due to its all-solid-state design, our UHV ADR mK STM is relatively simple, compact, and very modular. In particular, the mK stick, which carries the STM and the paramagnetic ADR pill, can be easily extracted from UHV without warming up the main LHe bath cryostat. We expect that this feature of our setup should make its further development and service simple, allowing for an efficient everyday operation. Although the current version of the mK stick is not bakeable due to the low thermal stability of the paramagnetic salt in the ADR pill, we show that this complication does not preclude work on atomically clean surfaces prepared in UHV. At the same time, the continuing discovery of new magnetocaloric materials makes the prospects of fully bakeable ADR setups reaching 100 mK very realistic.[52]

Another technical novelty demonstrated in this work is the successful use of the high-capacity cryopump as a substitute for mechanical pumping of the 1 K pot. We find that the cryopump's silent operation mode is essential for reaching the remarkable noise figures demonstrated in our measurements.

Finally, we showed that the lowest attainable effective electronic temperature of our STM junction is T_{eff} = 157 mK. This value is comparable with the data reported by other groups that use mK STMs based on dilution refrigerators. In our case, T_{eff} reacts weakly on the removal of high-frequency noise filters. One of the reasons may be the electromagnetic shielding of the laboratory.[33,34] A more detailed analysis of factors determining T_{eff} of our STM junction will be presented in upcoming publications.

ACKNOWLEDGMENTS

We acknowledge fruitful discussions with Josef Baumgartner (Entropy GmbH, Munich, Germany), Simon Chase (Chase Research Cryogenics Ltd., Sheffield, UK), Kurt Haselwimmer, Michael Krzyzowski (CryoVac GmbH and Co KG, Troisdorf, Germany), George Lecomte (GVL Cryoengineering GmbH, Stolberg, Germany), Gilbert G. Lonzarich (Cavendish Laboratory, University of Cambridge, UK), Jose Martinez Castro (PGI-3, Forschungszentrum Jülich), Stefan Stahl (Stahl-Electronics, Mettenheim, Germany), and Doreen Wernicke (Entropy GmbH, Munich, Germany). We also thank Werner Hürttlen, Jens Prigge, and Helmut Stollwerk for technical support. R.T. acknowledges support from the Young Investigator Group program (Grant No. VH-NG-514) of the Helmholtz Association.

DATA AVAILABILITY

The data that support the findings of this study are available from the corresponding author upon reasonable request.

REFERENCES

[1]Y. Niimi, H. Kambara, and H. Fukuyama, "Localized distributions of quasi-two-dimensional electronic states near defects artificially created at graphite surfaces in magnetic fields," Phys. Rev. Lett. **102**, 026803 (2009).

[2]Y. J. Song, A. F. Otte, Y. Kuk, Y. Hu, D. B. Torrance, P. N. First, W. A. de Heer, H. Min, S. Adam, M. D. Stiles, A. H. MacDonald, and J. A. Stroscio, "High-resolution tunnelling spectroscopy of a graphene quartet," Nature **467**, 185–189 (2010).

[3]N. Levy, T. Zhang, J. Ha, F. Sharifi, A. A. Talin, Y. Kuk, and J. A. Stroscio, "Experimental evidence for *s*-wave pairing symmetry in superconducting $Cu_xBi_2Se_3$ single crystals using a scanning tunneling microscope," Phys. Rev. Lett. **110**, 117001 (2013).

[4]M. Eltschka, B. Jäck, M. Assig, O. V. Kondrashov, M. A. Skvortsov, M. Etzkorn, C. R. Ast, and K. Kern, "Probing absolute spin polarization at the nanoscale," Nano Lett. **14**, 7171–7174 (2014).

[5]A. Roychowdhury, M. Dreyer, J. R. Anderson, C. J. Lobb, and F. C. Wellstood, "Microwave photon-assisted incoherent Cooper-pair tunneling in a Josephson STM," Phys. Rev. Appl. **4**, 034011 (2015).

[6]Z. Sun, M. Enayat, A. Maldonado, C. Lithgow, E. Yelland, D. C. Peets, A. Yaresko, A. P. Schnyder, and P. Wahl, "Dirac surface states and nature of superconductivity in noncentrosymmetric BiPd," Nat. Commun. **6**, 6633 (2015).

[7]B. Jäck, M. Eltschka, M. Assig, A. Hardock, M. Etzkorn, C. R. Ast, and K. Kern, "A nanoscale gigahertz source realized with Josephson scanning tunneling microscopy," Appl. Phys. Lett. **106**, 013109 (2015).

[8]C. R. Ast, B. Jäck, J. Senkpiel, M. Eltschka, M. Etzkorn, J. Ankerhold, and K. Kern, "Sensing the quantum limit in scanning tunnelling spectroscopy," Nat. Commun. **7**, 13009 (2016).

[9]B. Jäck, M. Eltschka, M. Assig, M. Etzkorn, C. R. Ast, and K. Kern, "Critical Josephson current in the dynamical Coulomb blockade regime," Phys. Rev. B **93**, 020504 (2016).

[10]F. D. Natterer, J. Ha, H. Baek, D. Zhang, W. G. Cullen, N. B. Zhitenev, Y. Kuk, and J. A. Stroscio, "Scanning tunneling spectroscopy of proximity superconductivity in epitaxial multilayer graphene," Phys. Rev. B **93**, 045406 (2016).

[11]M. H. Hamidian, S. D. Edkins, S. H. Joo, A. Kostin, H. Eisaki, S. Uchida, M. J. Lawler, E.-A. Kim, A. P. Mackenzie, K. Fujita, J. Lee, and J. C. S. Davis, "Detection of a Cooper-pair density wave in $Bi_2Sr_2CaCu_2O_{8+x}$," Nature **532**, 343–347 (2016).

[12]B. E. Feldman, M. T. Randeria, J. Li, S. Jeon, Y. Xie, Z. Wang, I. K. Drozdov, B. Andrei Bernevig, and A. Yazdani, "High-resolution studies of the Majorana atomic chain platform," Nat. Phys. **13**, 286–291 (2017).

[13]O. J. Clark, M. J. Neat, K. Okawa, L. Bawden, I. Marković, F. Mazzola, J. Feng, V. Sunko, J. M. Riley, W. Meevasana, J. Fujii, I. Vobornik, T. K. Kim, M. Hoesch, T. Sasagawa, P. Wahl, M. S. Bahramy, and P. D. C. King, "Fermiology and superconductivity of topological surface states in $PdTe_2$," Phys. Rev. Lett. **120**, 156401 (2018).

[14]T. Machida, Y. Sun, S. Pyon, S. Takeda, Y. Kohsaka, T. Hanaguri, T. Sasagawa, and T. Tamegai, "Zero-energy vortex bound state in the superconducting topological surface state of Fe(Se,Te)," Nat. Mater. **18**, 811–815 (2019).

[15]J. Senkpiel, J. C. Klöckner, M. Etzkorn, S. Dambach, B. Kubala, W. Belzig, A. L. Yeyati, J. C. Cuevas, F. Pauly, J. Ankerhold, C. R. Ast, and K. Kern, "Dynamical Coulomb blockade as a local probe for quantum transport," Phys. Rev. Lett. **124**, 156803 (2020).

[16]W. M. J. van Weerdenburg, M. Steinbrecher, N. P. E. van Mullekom, J. W. Gerritsen, H. von Allwörden, F. D. Natterer, and A. A. Khajetoorians, "A scanning tunneling microscope capable of electron spin resonance and pump-probe spectroscopy at mK temperature and in vector magnetic field," Rev. Sci. Instrum. **92**, 033906 (2021).

[17]K. P. Nuckolls, M. Oh, D. Wong, B. Lian, K. Watanabe, T. Taniguchi, B. A. Bernevig, and A. Yazdani, "Strongly correlated Chern insulators in magic-angle twisted bilayer graphene," Nature **588**, 610–615 (2020).

[18]M. Steinbrecher, W. M. J. van Weerdenburg, E. F. Walraven, N. P. E. van Mullekom, J. W. Gerritsen, F. D. Natterer, D. I. Badrtdinov, A. N. Rudenko, V. V. Mazurenko, M. I. Katsnelson, A. van der Avoird, G. C. Groenenboom, and A. A. Khajetoorians, "Quantifying the interplay between fine structure and geometry of an individual molecule on a surface," Phys. Rev. B **103**, 155405 (2021).

[19]N. Moussy, H. Courtois, and B. Pannetier, "A very low temperature scanning tunneling microscope for the local spectroscopy of mesoscopic structures," Rev. Sci. Instrum. **72**, 128–131 (2001).

[20]H. le Sueur and P. Joyez, "Room-temperature tunnel current amplifier and experimental setup for high resolution electronic spectroscopy in millikelvin scanning tunneling microscope experiments," Rev. Sci. Instrum. **77**, 123701 (2006).

[21]H. Kambara, T. Matsui, Y. Niimi, and H. Fukuyama, "Construction of a versatile ultralow temperature scanning tunneling microscope," Rev. Sci. Instrum. **78**, 073703 (2007).

[22]Y. J. Song, A. F. Otte, V. Shvarts, Z. Zhao, Y. Kuk, S. R. Blankenship, A. Band, F. M. Hess, and J. A. Stroscio, "Invited review article: A 10 mK scanning probe microscopy facility," Rev. Sci. Instrum. **81**, 121101 (2010).

[23]U. R. Singh, M. Enayat, S. C. White, and P. Wahl, "Construction and performance of a dilution-refrigerator based spectroscopic-imaging scanning tunneling microscope," Rev. Sci. Instrum. **84**, 013708 (2013).

[24]M. Assig, M. Etzkorn, A. Enders, W. Stiepany, C. R. Ast, and K. Kern, "A 10 mK scanning tunneling microscope operating in ultra high vacuum and high magnetic fields," Rev. Sci. Instrum. **84**, 033903 (2013).

[25]S. Misra, B. B. Zhou, I. K. Drozdov, J. Seo, L. Urban, A. Gyenis, S. C. J. Kingsley, H. Jones, and A. Yazdani, "Design and performance of an ultra-high vacuum scanning tunneling microscope operating at dilution refrigerator temperatures and high magnetic fields," Rev. Sci. Instrum. **84**, 103903 (2013).

[26]A. Roychowdhury, M. A. Gubrud, R. Dana, J. R. Anderson, C. J. Lobb, F. C. Wellstood, and M. Dreyer, "A 30 mK, 13.5 T scanning tunneling microscope with two independent tips," Rev. Sci. Instrum. **85**, 043706 (2014).

[27]H. von Allwörden, A. Eich, E. J. Knol, J. Hermenau, A. Sonntag, J. W. Gerritsen, D. Wegner, and A. A. Khajetoorians, "Design and performance of an ultra-high vacuum spin-polarized scanning tunneling microscope operating at 30 mK and in a vector magnetic field," Rev. Sci. Instrum. **89**, 033902 (2018).

[28]T. Machida, Y. Kohsaka, and T. Hanaguri, "A scanning tunneling microscope for spectroscopic imaging below 90 mK in magnetic fields up to 17.5 T," Rev. Sci. Instrum. **89**, 093707 (2018).

[29]T. Balashov, M. Meyer, and W. Wulfhekel, "A compact ultra-high vacuum scanning tunneling microscope with dilution refrigeration," Rev. Sci. Instrum. **89**, 113707 (2018).

[30]D. Wong, S. Jeon, K. P. Nuckolls, M. Oh, S. C. J. Kingsley, and A. Yazdani, "A modular ultra-high vacuum millikelvin scanning tunneling microscope," Rev. Sci. Instrum. **91**, 023703 (2020).

[31]J. Schwenk, S. Kim, J. Berwanger, F. Ghahari, D. Walkup, M. R. Slot, S. T. Le, W. G. Cullen, S. R. Blankenship, S. Vranjkovic, H. J. Hug, Y. Kuk, F. J. Giessibl, and J. A. Stroscio, "Achieving μeV tunneling resolution in an *in-operando* scanning tunneling microscopy, atomic force microscopy, and magnetotransport system for quantum materials research," Rev. Sci. Instrum. **91**, 071101 (2020).

[32]F. Pobell, *Matter and Methods at Low Temperatures* (Springer-Verlag Berlin Heidelberg, 2007).

[33]B. Voigtländer, P. Coenen, V. Cherepanov, P. Borgens, T. Duden, and F. S. Tautz, "Low vibration laboratory with a single-stage vibration isolation for microscopy applications," Rev. Sci. Instrum. **88**, 023703 (2017).

[34]See http://www.ets-lindgren.com/products/shielding for ETS-Lindgren.

[35]VAb Vakuum-Anlagenbau GmbH, Marie-Curie-Str. 11, 25337 Elmshorn, Germany.

[36]Model FDG 150, FOCUS GmbH, Neukirchner Str. 2, 65510 Huenstetten, Germany.

[37]Model ErLEED 150, SPECS Surface Nano Analysis GmbH, Voltastrasse 5, 13355 Berlin, Germany.

[38]VACOM Vakuum Komponenten & Messtechnik GmbH, In den Brückenäckern, 307751 Großlöbichau, Germany.

[39]Model 242-SMAD50-C40-4, Allectra GmbH, Traubeneichenstr. 62-66, 16567 Schönfliess, Germany.

[40]Model NEXTorr Z100, SAES Getters S.p.A., Viale Italia 77, 20045 Lainate, Italy.

[41] CryoVac GmbH & Co KG, Heuserweg 14, 53842 Troisdorf, Germany.
[42] Cryomagnetics, Inc., 1006 Alvin Weinberg Drive, Oak Ridge, TN 37830, USA.
[43] R. Haefer, *Cryopumping: Theory and Practice* (Clarendon Press, 1989).
[44] A. D. Shvets, "The use of liquid helium-3 to obtain temperatures down to 0.3 K," Cryogenics **6**, 333–337 (1966).
[45] J. P. Torre and G. Chanin, "Miniature liquid ^{3}He refrigerator," Rev. Sci. Instrum. **56**, 318–320 (1985).
[46] Chase Research Cryogenics Ltd., Unit 2, Neepsend Industrial Estate, 80 Parkwood Rd, Neepsend, Sheffield S3 8AG, UK.
[47] Entropy GmbH, Gmunder Str. 37a, 81379 Munich, Germany.
[48] Lake Shore Cryotronics, Inc., 550 Tressler Dr., Westerville, OH 43082, USA.
[49] CMR-Direct, Willow House, 100 High Street, Somersham PE28 3EH, UK.
[50] Type GVLZ141, GVL Cryoengineering Dr. George V. Lecomte GmbH, Aachener Strasse 89, 52223 Stolberg, Germany.
[51] G. W. Wilson and P. T. Timbie, "Construction techniques for adiabatic demagnetization refrigerators using ferric ammonium alum," Cryogenics **39**, 319–322 (1999).
[52] D. Jang, T. Gruner, A. Steppke, K. Mitsumoto, C. Geibel, and M. Brando, "Large magnetocaloric effect and adiabatic demagnetization refrigeration with $YbPt_2Sn$," Nat. Commun. **6**, 8680 (2015).
[53] P. Wikus, G. Burghart, and E. Figueroa-Feliciano, "Optimum operating regimes of common paramagnetic refrigerants," Cryogenics **51**, 555–558 (2011).
[54] O. E. Vilches and J. C. Wheatley, "Measurements of the specific heats of three magnetic salts at low temperatures," Phys. Rev. **148**, 509–516 (1966).
[55] J. P. Torre and G. Chanin, "Heat switch for liquid-helium temperatures," Rev. Sci. Instrum. **55**, 213–215 (1984).
[56] P. Schiffer, A. P. Ramirez, D. A. Huse, and A. J. Valentino, "Investigation of the field induced antiferromagnetic phase transition in the frustrated magnet: Gadolinium gallium garnet," Phys. Rev. Lett. **73**, 2500–2503 (1994).
[57] Model SA-606F2, NF Corporation, 6-3-20 Tsunashima Higashi, Kohoku-ku, Yokohama 223-8508, Japan.
[58] Nanonis SPM control system, SPECS Zurich GmbH, Technoparkstrasse 1, 8005 Zurich, Switzerland.
[59] Model 51-726-017, API Technologies Spectrum Control GmbH, Hansastrasse 6, 91126 Schwabach, Germany.
[60] Tusonix/CTS 4106-001LF, Mouser part number 800-4106-001LF, 1000 N. Main Street, Mansfield, TX 76063, USA.
[61] Model DLPCA-200, FEMTO Messtechnik GmbH, Klosterstr. 64, 10179 Berlin, Germany.